phys. stat. sol. (b) **108**, 363 (1981)

Subject classification: 13.4 and 19; 22.1.2

Institute for the Study of Defects in Solids, Department of Physics, State University of New York at Albany[1]) *(a) and Natuurkundig Laboratorium der Universiteit van Amsterdam*[2]) *(b)*

EPR Observation of an Au–Fe Complex in Silicon

I. Experimental Data

By

R. L. KLEINHENZ (a), Y. H. LEE[3]) (a), J. W. CORBETT (a),
E. G. SIEVERTS (b), S. H. MULLER (b), and C. A. J. AMMERLAAN (b)

After quenching of Au-doped FZ silicon an anisotropic axially symmetric EPR spectrum is observed. The spectrum exhibits a hyperfine interaction with ^{197}Au nuclei ($I = \frac{3}{2}$). In samples which were intentionally doped with isotopically enriched ^{57}Fe ($I = \frac{1}{2}$) an additional hyperfine interaction with this nucleus is observed. Due to the large nuclear electric quadrupole moment of ^{197}Au the nuclear quadrupole interaction strongly influences the EPR spectrum. From this effect a lower limit for the quadrupole interaction can be derived by a computer diagonalization of the spin Hamiltonian. From the observed hyperfine interactions and the known properties of Fe and Au in silicon it is concluded that this spectrum originates from a [Au_sFe_i] complex.

Ein anisotropes axialsymmetrisches Spektrum wird in ZF-Siliziumproben, die mit Gold dotiert und abgeschreckt waren, beobachtet. Das Spektrum zeigt Hyperfeinwechselwirkung mit Goldatomkernen ($I = \frac{3}{2}$). Proben, die zusätzlich mit dem Eisenisotop ^{57}Fe ($I = \frac{1}{2}$) dotiert wurden, zeigen eine weitere Hyperfeinwechselwirkung mit diesen Atomkernen. Wegen des großen Quadrupolmomentes von ^{197}Au ist das Spektrum stark beeinflußt von der Quadrupolwechselwirkung. Der Spin-Hamiltonoperator wird vom Computer diagonalisiert und eine untere Grenze für den Quadrupolwechselwirkungsparameter abgeleitet. Aus der beobachteten Hyperfeinstruktur und den bekannten Eigenschaften von Fe und Au wird geschlossen, daß dieses Spektrum von einem [Au_sFe_i]-Komplex stammt.

1. Introduction

Gold is an important impurity in silicon and is widely used in the manufacturing technology to control lifetimes. Deep donor and acceptor levels of Au and their capture cross-sections have been studied for many years using electrical/optical

Table 1
Solubilities and diffusion coefficients from Wilcox and LaChapelle [11]

interstitial gold solubility	at 1200 °C	1.5×10^{16} cm^{-3}
	at 1000 °C	6.5×10^{14} cm^{-3}
substitutional gold solubility	at 1200 °C	7.7×10^{16} cm^{-3}
	at 1000 °C	8.7×10^{15} cm^{-3}
interstitial gold diffusion coefficient	at 1200 °C	2.3×10^{-5} cm^2 s^{-1}
substitutional gold diffusion coefficient	at 1200 °C	2.9×10^{-10} cm^2 s^{-1}

[1]) Albany, NY 12222, USA.
[2]) Valckenierstraat 65, 1018 XE Amsterdam, The Netherlands.
[3]) Present address: IBM, Thomas J. Watson Research Center, P.O. Box 218, Yorktown Heights, NY 10598, USA.

measurements [1 to 7]. An acceptor level is generally found around $E_c - 0.55$ eV, a donor level around $E_v + 0.35$ eV. The diffusion of gold in silicon is thought to occur by means of the dissociative mechanism first developed by Frank and Turnbull [8] and generalized by Sturge [9]; the application of this mechanism to gold diffusion in silicon was first suggested by Dash [10]. Wilcox and LaChapelle [11] studied the diffusion and solid solubility of gold in silicon. Their data are shown in Table 1.

Gold is generally accepted to be incorporated substitutionally in the silicon lattice. In the highly successful model by Ludwig and Woodbury [12], extended to the 5d shell, the ground state configuration for electrically neutral substitutional gold in silicon is $5d^76(sp^3)$, having an effective orbital singlet, a spin $S = \frac{3}{2}$, and therefore $J = \frac{3}{2}$; so there ought to be EPR information available. The EPR on isolated gold in silicon has been reported only once recently by Höhne [13] who interpreted his spectrum, Au(1), as interstitial gold (see below, however). Pairs formed by gold with the acceptors manganese and chromium were found by Ludwig and Woodbury [12].

Iron is also an important impurity in silicon. It diffuses interstitially in silicon with a diffusion constant of about $7 \times 10^{-6}\,cm^2 s^{-1}$ at 1200 °C [14]. Solubility of iron in silicon is about $5 \times 10^{15}\,cm^{-3}$ at 1200 °C [14]. Upon quenching from a high temperature iron is frozen in a tetrahedral interstitial site. Interest in iron contamination has recently been re-awakened by the identification of the iron interstitial as a "thermal defect" [15]; it was found that after a high-temperature heat treatment (1200 °C) iron is present in most silicon samples, as interstitial iron can be observed after a fast quench by EPR and DLTS [15, 16]. Its energy level in the band gap is $E_v + 0.4$ eV. Because of its low migration energy of 0.69 eV [15], the iron interstitial diffuses even at room temperature to form precipitates. Arguments have been made for iron to be either an intrinsic [17] or an extrinsic defect [18], and ways to avoid it altogether are being sought [19]. Ludwig and Woodbury [12] studied iron by EPR. Interstitial iron gives rise to a single isotropic line at $g = 2.070$. They also found that iron forms pairs with the acceptors boron, gallium, and indium.

In previous publications [17, 20] we reported a new spectrum, A23, for a gold–iron pair. A similar spectrum was also reported recently by Höhne [13] who thought it to be single interstitial gold. We have now analyzed the spectrum completely and have proved the presence of iron by hyperfine interaction with ^{57}Fe. In Part II we analyze the hyperfine interaction further in terms of electron configuration.

2. Experimental

The samples were n- and p-type silicon with resistivities from 0.5 to 100 Ωcm. Gold was diffused into the sample by enclosing the sample together with a piece of thin gold wire in a quartz capsule under an argon atmosphere. The capsule was then heated at 1200 °C for from 30 min to 16 h and quenched by immersion of the capsule into water. This treatment always introduces Fe_i°. Some samples were enriched with ^{57}Fe by either coating with an ^{57}Fe-enriched $FeCl_2$ solution [21] or by ion implantation with ^{57}Fe. In the former case a 90% enrichment was achieved, in the latter 82%. After both diffusion steps of the $FeCl_2$-coated samples, these samples were ground and etched before a short final heating and quenching, in order to remove internal stresses [21].

Spectra were measured on a Varian V4500 homodyne spectrometer operating at X-band in Albany and on a K-band spectrometer with superheterodyne detection in Amsterdam. The measurements were taken at 4.2 K in dispersion mode.

3. Results

3.1 EPR Spectrum

In addition to the Fe_i^0 line at $g = 2.070$, a spectrum was observed at 4.2 K measuring temperature, in some cases immediately after quenching. This spectrum was previously labelled A23. It is axially symmetric with tirigonal symmetry. Hyperfine interaction with the Au nucleus ($I = \frac{3}{2}$) causes a fourfold splitting. In the $g_{\|}$ direction ($\boldsymbol{B} \| [111]$) this splitting is equidistant. In the $g_{\perp}$ direction, however, the splitting is not even at all, in fact the $I = +\frac{3}{2}$ and the $I = -\frac{3}{2}$ lines coincide. This is due to an electric quadrupole interaction with the Au nucleus. The samples enriched with ^{57}Fe show an additional twofold splitting of each line due to the hyperfine interaction with the ^{57}Fe nucleus ($I = \frac{1}{2}$). This splitting is anisotropic and also has $\langle 111 \rangle$ symmetry. The additional splitting in the ^{57}Fe enriched samples is illustrated in the spectra of Fig. 1a, b. Small hyperfine shoulders due to ^{29}Si were also observed, but could not be resolved. The observed width of the EPR lines at half height was approximately 0.15 mT.

3.2 Analysis of the spectrum

The spectrum can be analyzed with an effective spin Hamiltonian

$$\mathcal{H} = \mu_B \boldsymbol{B} \cdot \mathbf{g} \cdot \boldsymbol{S} + \boldsymbol{I}_{Au} \cdot \mathbf{A}_{Au} \cdot \boldsymbol{S} + \boldsymbol{I}_{Au} \cdot \mathbf{Q} \cdot \boldsymbol{I}_{Au} \, (+ \boldsymbol{I}_{Fe} \cdot \mathbf{A}_{Fe} \cdot \boldsymbol{S}) \tag{1}$$

with an effective spin $S = \frac{1}{2}$.

Bleaney [22] and Abragam and Bleaney [23] gave a perturbation treatment for the case of a quadrupole term small compared with the hyperfine splitting for $\boldsymbol{B} \| \boldsymbol{g}_{\perp}$. Their treatment, however, was not sufficient in our case. Muha [24] and Vugman et al. [25] recently also treated the general case for arbitrary relative size of the hyperfine and quadrupolar parameters for $S = \frac{1}{2}$, $I = \frac{3}{2}$, also for $\boldsymbol{B} \| \boldsymbol{g}_{\perp}$. Here we present a very simple perturbation treatment for the case $Q \gg A$, $S = \frac{1}{2}$, $I = \frac{3}{2}$, $\boldsymbol{B} \| \boldsymbol{g}_{\perp}$.

While Muha [24] takes linear combinations of $|m_S m_I\rangle$ functions with m differing by two, we take linear combinations of $|m_S m_I\rangle$ functions with the same absolute value of m_I to form eight basis functions,

$$\left.\begin{aligned}
\psi_1 &= \tfrac{1}{2}\{|\tfrac{1}{2}\,\tfrac{3}{2}\rangle + |\tfrac{1}{2}\,-\tfrac{3}{2}\rangle + |-\tfrac{1}{2}\,\tfrac{3}{2}\rangle + |-\tfrac{1}{2}\,-\tfrac{3}{2}\rangle\}\,, \\
\psi_2 &= \tfrac{1}{2}\{|\tfrac{1}{2}\,\tfrac{1}{2}\rangle + |\tfrac{1}{2}\,-\tfrac{1}{2}\rangle + |-\tfrac{1}{2}\,\tfrac{1}{2}\rangle + |-\tfrac{1}{2}\,-\tfrac{1}{2}\rangle\}\,, \\
\psi_3 &= \tfrac{1}{2}\{|\tfrac{1}{2}\,\tfrac{1}{2}\rangle - |\tfrac{1}{2}\,-\tfrac{1}{2}\rangle - |-\tfrac{1}{2}\,\tfrac{1}{2}\rangle + |-\tfrac{1}{2}\,-\tfrac{1}{2}\rangle\}\,, \\
\psi_4 &= \tfrac{1}{2}\{|\tfrac{1}{2}\,\tfrac{3}{2}\rangle - |\tfrac{1}{2}\,-\tfrac{3}{2}\rangle - |-\tfrac{1}{2}\,\tfrac{3}{2}\rangle + |-\tfrac{1}{2}\,-\tfrac{3}{2}\rangle\}\,, \\
\psi_5 &= \tfrac{1}{2}\{|\tfrac{1}{2}\,\tfrac{3}{2}\rangle - |\tfrac{1}{2}\,-\tfrac{3}{2}\rangle + |-\tfrac{1}{2}\,\tfrac{3}{2}\rangle - |-\tfrac{1}{2}\,-\tfrac{3}{2}\rangle\}\,, \\
\psi_6 &= \tfrac{1}{2}\{|\tfrac{1}{2}\,\tfrac{1}{2}\rangle - |\tfrac{1}{2}\,-\tfrac{1}{2}\rangle + |-\tfrac{1}{2}\,\tfrac{1}{2}\rangle - |-\tfrac{1}{2}\,-\tfrac{1}{2}\rangle\}\,, \\
\psi_7 &= \tfrac{1}{2}\{|\tfrac{1}{2}\,\tfrac{1}{2}\rangle + |\tfrac{1}{2}\,-\tfrac{1}{2}\rangle - |-\tfrac{1}{2}\,\tfrac{1}{2}\rangle - |-\tfrac{1}{2}\,-\tfrac{1}{2}\rangle\}\,, \\
\psi_8 &= \tfrac{1}{2}\{|\tfrac{1}{2}\,\tfrac{3}{2}\rangle + |\tfrac{1}{2}\,-\tfrac{3}{2}\rangle - |-\tfrac{1}{2}\,\tfrac{3}{2}\rangle - |-\tfrac{1}{2}\,-\tfrac{3}{2}\rangle\}\,.
\end{aligned}\right\} \tag{2}$$

For $\boldsymbol{B} \| \boldsymbol{g}_{\perp}$ the Hamiltonian (1) reduces to

$$\mathcal{H} = \mathcal{H}_0 + \mathcal{H}_{\text{pert}}$$

with

$$\left.\begin{aligned}
\mathcal{H}_0 &= g_{\perp}\mu_B B S_x + P[3I_z^2 - I(I+1)]\,, \\
\mathcal{H}_{\text{pert}} &= \tfrac{1}{2} A_{\perp}(S^+ I^- + S^- I^+) + A_{\|} S_z I_z\,.
\end{aligned}\right\} \tag{3}$$

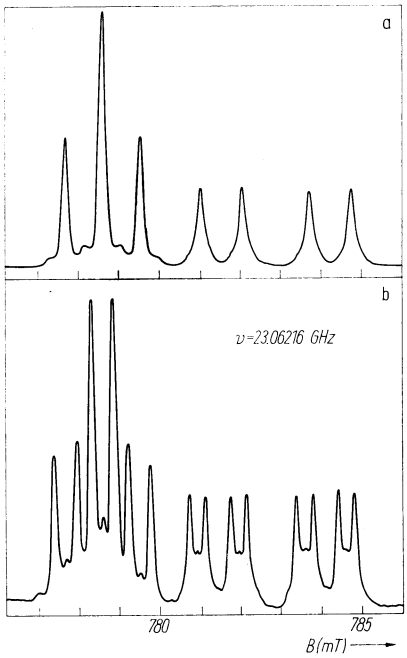

Fig. 1

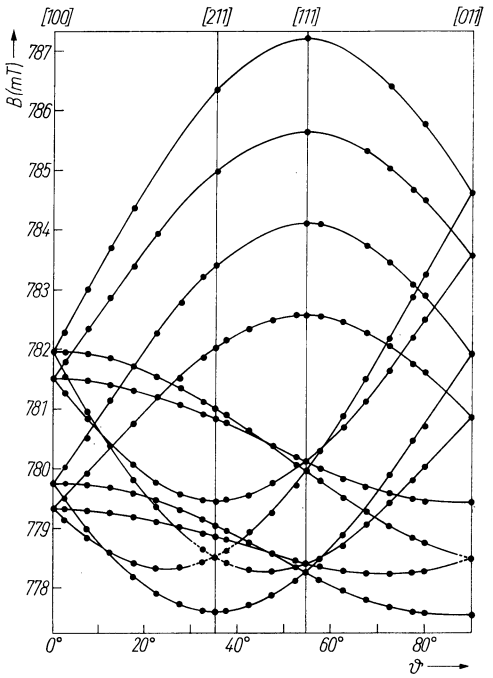

Fig. 2

Fig. 1. Experimental spectra at K band of A23 for $\boldsymbol{B}$ || [011]. Spectrum a) is of a sample with natural iron, b) is of a sample that was enriched with ^{57}Fe and shows the additional ^{57}Fe ($I = \frac{1}{2}$) hyperfine splitting

Fig. 2. Angular dependence of EPR line positions for the A23 spectrum at K band. The solid dots are the experimental data points

Here P is defined by

$$\mathbf{Q} = \begin{pmatrix} -P & 0 & 0 \\ 0 & -P & 0 \\ 0 & 0 & 2P \end{pmatrix}$$

and A is short for A_{Au}. The functions shown in (2) are eigenfunctions of $\mathcal{H}_0$. With these basis functions the Hamiltonian matrix reduces to two 4×4 blocks along the diagonal, the rest being zero. Within either block no degeneracies occur, and it is possible to apply second-order perturbation theory which yields the energy levels as shown in (4):

$$\left.\begin{aligned}
E_1 &= \tfrac{1}{2} g_\perp \mu_B B + 3P + A_\perp^2/32P\,, \\
E_2 &= \tfrac{1}{2} g_\perp \mu_B B - 3P - A_\perp^2/32P + A_\perp/2\,, \\
E_3 &= -\tfrac{1}{2} g_\perp \mu_B B - 3P - A_\perp^2/32P + A_\perp/2\,, \\
E_4 &= -\tfrac{1}{2} g_\perp \mu_B B + 3P + A_\perp^2/32P\,, \\
E_5 &= \tfrac{1}{2} g_\perp \mu_B B + 3P + A_\perp^2/32P\,, \\
E_6 &= \tfrac{1}{2} g_\perp \mu_B B - 3P - A_\perp^2/32P - A_\perp/2\,, \\
E_7 &= -\tfrac{1}{2} g_\perp \mu_B B - 3P - A_\perp^2/32P - A_\perp/2\,, \\
E_8 &= -\tfrac{1}{2} g_\perp \mu_B B + 3P + A_\perp^2/32P\,.
\end{aligned}\right\} \qquad (4)$$

Terms of the order $1/B$ and higher are neglected.

EPR transitions occur between the energy levels 1–8, 2–7, 3–6, and 4–5 with the energies

$$\left.\begin{aligned} \Delta E_{1,8} &= g_{\perp}\mu_{\mathrm{B}}B\,, \qquad \Delta E_{2,7} = g_{\perp}\mu_{\mathrm{B}}B + A_{\perp}\,, \\ \Delta E_{3,6} &= g_{\perp}\mu_{\mathrm{B}}B - A_{\perp}\,, \qquad \Delta E_{4,5} = g_{\perp}\mu_{\mathrm{B}}B\,. \end{aligned}\right\} \tag{5}$$

These transition energies are independent of Q for the case $Q \gg A$, and the $I = +\frac{3}{2}$ and $I = -\frac{3}{2}$ lines coincide. This is illustrated by the spectrum in Fig. 1a for $\boldsymbol{B} \parallel [011]$ The three low-field EPR lines originate from defect orientations for which the magnetic field is parallel to $\boldsymbol{g}_{\perp}$. The $I = \pm\frac{3}{2}$ lines coincide to give a central line of double intensity. (The m_I labels are of course not a good quantum number anymore, but it is convenient to label the lines this way. At least for $\boldsymbol{B} \parallel \boldsymbol{g}_{\parallel}$, m_I is a good quantum number, and we keep this label m_I for the line through the full 180° rotation.) $A_{\perp}$ can be read off the spectrum in the $g_{\perp}$ direction directly. $A_{\parallel}$ can be obtained from the spectrum in the $g_{\parallel}$ direction where the quadrupole effects vanish and the transition energies are

$$\Delta E(m_I) = g_{\parallel}\mu_{\mathrm{B}}B + m_I A_{\parallel}\,. \tag{6}$$

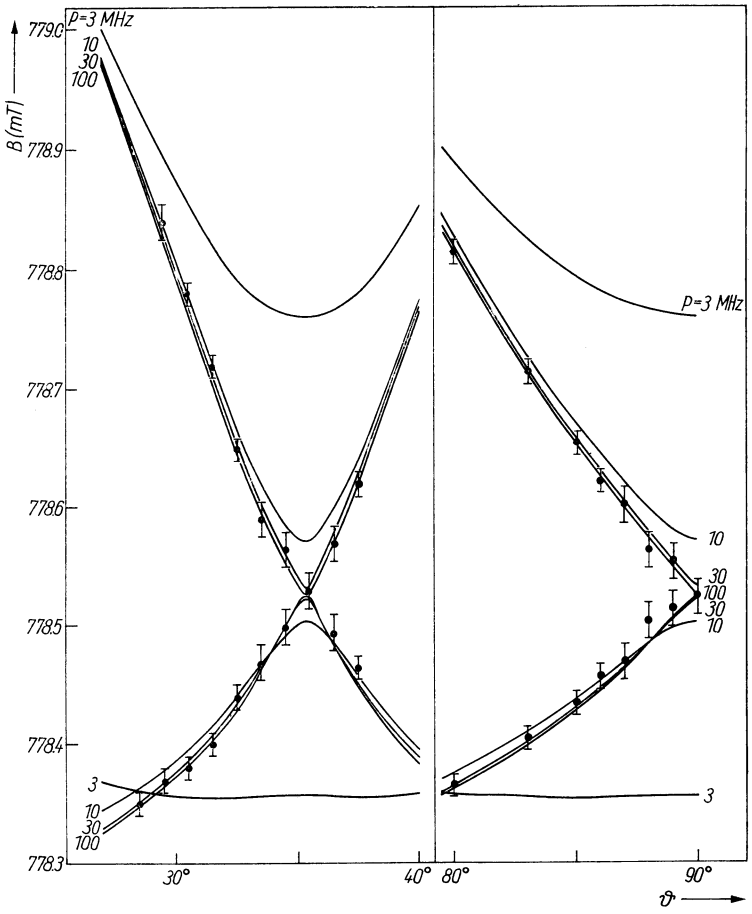

Fig. 3. Details of the K band rotation pattern near $\boldsymbol{g}_{\perp}$ for various values of P

Because a perturbation treatment is not possible for the general direction of $\boldsymbol{B}$ the Hamiltonian has to be solved numerically by a computer. With a least-squares fit of the data points to the Hamiltonian (1) we found the values of g and A. P was not entered as a free parameter in the least-squares fit but rather was kept constant, the reason for this being that for large values of P the rotation pattern shows little or no dependence on P even for directions other than $\boldsymbol{B} \parallel \boldsymbol{g}_{\parallel}$. For our experimental data it turned out that in the calculation the least-squares sum was practically independent of P, so that this value could not be simply determined. By substituting several values for P the lines in Fig. 3 were calculated, and by comparison with the experimental data points we could assign a lower limit to P. Fig. 2 shows the experimental data points and the fitted rotation pattern. Details of the rotation pattern around $\boldsymbol{g}_{\perp}$ for a number of values of P are shown in Fig. 3. The parameters we found are shown in Table 2 and are compared with the parameters found by Höhne for his Au(1).

A23 and Au(1) are formed and observed under very similar conditions. Apart from a slight difference in g-values the parameters of the spin-Hamiltonian are the same

Table 2

EPR parameters for the Au–Fe pair (A23) and Höhne's Au(1) [13]

	A23	Au(1) [13]
$g_{\parallel}$	2.0993 ± 0.0002	2.1005 ± 0.0003
$g_{\perp}$	2.1165 ± 0.0002	2.1183 ± 0.0003
$A_{\parallel}^{\mathrm{Au}}$	$(15.1 \pm 0.2) \times 10^{-4}\ \mathrm{cm}^{-1} = (45.3 \pm 0.5)$ MHz	$(15.4 \pm 0.5) \times 10^{-4}\ \mathrm{cm}^{-1}$
$A_{\perp}^{\mathrm{Au}}$	$(9.2 \pm 0.2) \times 10^{-4}\ \mathrm{cm}^{-1} = (27.5 \pm 0.5)$ MHz	$(9.6 \pm 0.5) \times 10^{-4}\ \mathrm{cm}^{-1}$
P*)	$> 5 \times 10^{-4}\ \mathrm{cm}^{-1} = 15$ MHz	$> 20 \times 10^{-4}\ \mathrm{cm}^{-1}$
$A_{\parallel}^{\mathrm{Fe}}$	$(3.3 \pm 0.2) \times 10^{-4}\ \mathrm{cm}^{-1} = (10.0 \pm 0.5)$ MHz	—
$A_{\perp}^{\mathrm{Fe}}$	$(5.6 \pm 0.2) \times 10^{-4}\ \mathrm{cm}^{-1} = (16.9 \pm 0.5)$ MHz	—
A^{Si}	$\lessapprox 5 \times 10^{-4}\ \mathrm{cm}^{-1} = 15$ MHz	$\lessapprox 5 \times 10^{-4}\ \mathrm{cm}^{-1}$

*) Note that Höhne [13] defines P differently for Au(1). In his notation we would have $P < < 15 \times 10^{-4}\ \mathrm{cm}^{-1}$ for A23.

within the error limits. (The difference in g-value translates at X-band into a field difference of only about 0.16 mT.) Therefore we are inclined to think that in fact A23 and Au(1) are the same.

Detailed calculations around $\boldsymbol{g}_{\perp}$ showed that in the limit $P \gg A$ the lines have a sharp kink at the $\boldsymbol{g}_{\perp}$ direction where they touch, or, as it can be viewed, an actual crossing occurs (see Fig. 2 and 3). This degeneracy is reflected in our choice of basis functions where we mix equal amounts of $I = +\frac{3}{2}$ and $I = -\frac{3}{2}$ functions together.

The hyperfine tensor $\mathbf{A}$ is often written as

$$\mathbf{A} = a\mathbf{1} + \mathbf{B}$$

with

$$\mathbf{B} = \begin{pmatrix} -b & 0 & 0 \\ 0 & -b & 0 \\ 0 & 0 & 2b \end{pmatrix}.$$

Here $a\mathbf{1}$ is the Fermi contact term and $\mathbf{B}$ the dipole–dipole term. In this notation the

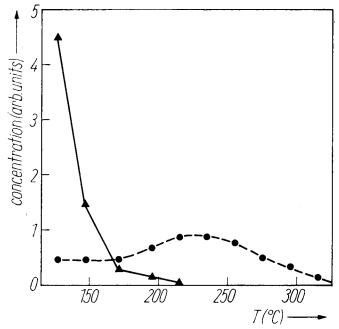

Fig. 4. Annealing characteristics of A23 (●) and Fe_i^0 (▲)

hyperfine values for Au and ^{57}Fe are

$$a_{Au} = (11.1 \pm 0.2) \times 10^{-4}\ cm^{-1} = (33.4 \pm 0.5)\ MHz\ ,$$
$$b_{Au} = (2.0 \pm 0.2) \times 10^{-4}\ cm^{-1} = (6.0 \pm 0.5)\ MHz\ ,$$
$$a_{Fe} = (4.9 \pm 0.2) \times 10^{-4}\ cm^{-1} = (14.6 \pm 0.5)\ MHz\ ,$$
$$b_{Fe} = (-0.8 \pm 0.2) \times 10^{-4}\ cm^{-1} = (-2.3 \pm 0.5)\ MHz\ .$$

The absolute signs of the hyperfine parameters cannot be determined. What is important above (and will be used in Part II) is that for the gold hyperfine interaction a and b are of the same sign, while for iron a and b are of opposite signs.

3.3 Annealing characteristics

The center is already present with low intensity in some samples right after the quench. Its intensity increases upon annealing around 200 °C. Around 300 °C it disappears. An isochronal annealing curve is shown in Fig. 4. The annealing time of each step was 10 min. The sample was phosphorus-doped float zone material with a resistivity of 10 Ωcm.

4. Discussion and Model

The spectrum A23 was interpreted tentatively as an [Au–Fe] complex by Lee et al. [17]. Höhne [13] reported the same spectrum he called Au(1) which he thought to be single interstitial Au. Our hyperfine structure results with ^{57}Fe clearly indicate the involvement of iron in A23. Gold is generally assumed to be incorporated in the silicon lattice on a substitutional site. Iron is known to diffuse interstitially, and to reside in an interstitial site after a quench from high temperature. This, together with the trigonal symmetry of A23, points towards a substitutional gold with an iron on a nearest tetrahedral interstitial site, or at least along a [111] axis from the gold.

Further evidence is gained from the formation kinetics. The appearance of A23 is linked to the disappearance of the interstitial iron line, which anneals out at 200 °C, but disappears slowly even at room temperature. A sample that had gold diffused in, was quenched and initially showed no A23, did so after one month at room temperature. In samples that were quenched somewhat slowly, A23 was already observed right after the quench.

Ludwig and Woodbury [12] interpreted the pairs that they found as a transition metal ion occupying the nearest interstitial site to a substitutional acceptor ion. Interstitial iron is a donor at $E_v + 0.4$ eV, while substitutional gold may be either a donor at $E_v + 0.35$ eV, slightly below the iron level, or an acceptor at $E_c - 0.55$ eV,

slightly above the iron level. But gold is much more electronegative than iron; on the Pauling scale, the value for gold is 2.4, the value for iron 1.8. This makes the transfer of one electron from the iron to the gold likely, making the center $[Au_s^- Fe_i^+]$. This ionicity could be the attractive force between the fixed substitutional gold and an interstitially diffusing iron. It may also distort the iron from its natural tetrahedral interstitial site along the [111] direction towards the gold. If we accept the interpretation $[Au_s^- Fe_i^+]$ we can also account for the spin state of this center in the highly successful model by Ludwig and Woodbury [12] extended to the 5d shell and trigonal symmetry; according to the model Au_s^- has an electronic configuration of $5d^8 6sp^3$, which in trigonal symmetry is an orbital singlet and has an electronic spin $S = 1$. Therefore, $J = 1$ for Au_s^-. Fe_i^+ has a configuration $3d^7$. In trigonal symmetry it has no orbital angular momentum. Its spin $S = \frac{3}{2}$, therefore $J = \frac{3}{2}$.

Combining the Au_s^- spin of 1 and the Fe_i^+ spin of $\frac{3}{2}$ gives a total $J = \frac{1}{2}$, $\frac{3}{2}$, or $\frac{5}{2}$. Our spectrum can be interpreted with an effective spin $J = \frac{1}{2}$. A detailed discussion of the electronic structure follows in Part II. A recent study of the thermal and optical properties of gold-related deep levels in silicon by Lang et al. [7] points out the complex nature of such defects. It concludes that deep levels due to gold in silicon must be associated with some sort of complex structure rather than be viewed as just simple substitutional Shockley-Read-Hall deep levels. The pair formation of gold with such a common (often accidental) impurity as iron that we report here supports that conclusion. Gold apparently can be present in many forms, probably paired with other defects and impurities.

5. Summary

After gold diffusion followed by a fast quench and a low-temperature anneal we observe a spectrum, A23. Hyperfine interaction with the nuclear spin of ^{197}Au ($I = \frac{3}{2}$, natural abundance 100%) and the nuclear spin of ^{57}Fe ($I = \frac{1}{2}$, natural abundance 2.25%) prove that both gold and iron are involved in the center. On grounds of electronic configurations we propose the model $[Au_s^- Fe_i^+]$. This interpretation is underlined by the formation kinetics.

Acknowledgement

We like to thank G. M. Tuynman who developed a computer library for the analysis of EPR spectra.

References

[1] C. B. COLLINS, R. O. CARLSON, and C. J. GALLAGHER, Phys. Rev. **105**, 1168 (1957).
[2] K. D. GLINCHUK and N. M. LITOVCHENKO, Soviet Phys. — Solid State **6**, 2963 (1965).
[3] L. D. YAU and C. T. SAH, Appl. Phys. Letters **21**, 157 (1972).
[4] O. ENGSTRÖM and H. G. GRIMMEISS, Appl. Phys. Letters **25**, 413 (1974); J. appl. Phys. **46**, 831 (1975).
[5] D. C. WONG and C. M. PENCHINA, Phys. Rev. B **12**, 5840 (1975).
[6] S. D. BROTHERTON and J. BICKNELL, J. appl. Phys. **49**, 667 (1978).
[7] D. V. LANG, H. G. GRIMMEISS, E. MEIJER, and M. JAROS, Phys. Rev. B **22**, 3917 (1980).
[8] F. C. FRANK and D. TURNBULL, Phys. Rev. **104**, 617 (1956).
[9] M. D. STURGE, Proc. Phys. Soc. **73**, 297 (1959).
[10] W. C. DASH, J. appl. Phys. **31**, 2275 (1960).
[11] W. R. WILCOX and T. J. LACHAPELLE, J. appl. Phys. **35**, 240 (1964).
[12] G. W. LUDWIG and H. H. WOODBURY, Solid State Phys. **13**, 223 (1962).
[13] M. HÖHNE, phys. stat. sol. (b) **99**, 651 (1980).
[14] J. D. STRUTHERS, J. appl. Phys. **27**, 1560 (1956).

[15] Y. H. Lee, R. L. Kleinhenz, and J. W. Corbett, Appl. Phys. Letters **31**, 142 (1977).
[16] J. D. Gerson, L. J. Cheng, and J. W. Corbett, J. appl. Phys. **48**, 4821 (1977).
[17] Y. H. Lee, R. L. Kleinhenz, and J. W. Corbett, Inst. Phys. Conf. Ser. **46**, 521 (1978).
[18] E. Weber and H. G. Riotte, Appl. Phys. Letters **33**, 433 (1978); J. appl. Phys. **51**, 1484 (1980).
[19] H. J. Rijks, J. Bloem, and L. J. Giling, J. appl. Phys. **50**, 1370 (1979).
[20] R. L. Kleinhenz, Y. H. Lee, E. G. Sieverts, and J. W. Corbett, Bull. Amer. Phys. Soc. **25**, 325 (1980).
[21] S. H. Muller, Ph. D. Thesis, University of Amsterdam, 1981.
[22] B. Bleaney, Phil. Mag. **42**, 441 (1951).
[23] A. Abragam and B. Bleaney, Electron Paramagnetic Resonance of Transition Ions, Clarendon Press, Oxford 1970 (Chap. 3).
[24] G. M. Muha, J. magnetic Res. **32**, 121 (1978).
[25] N. V. Vugman, A. O. Caride, and S. I. Zanette, Mol. Phys. **35**, 715 (1978).

(Received May 19, 1981)